# Cellular memory in eukaryotic chemotaxis depends on the background chemoattractant concentration

Richa Karmakar, Man-Ho Tang, Haicen Yue, Daniel Lombardo, Aravind Karanam, Brian A. Camley, Alex Groisman, and Wouter-Jan Rappel

Phys. Rev. E **103**, 012402 — Published 6 January 2021

DOI: 10.1103/PhysRevE.103.012402

# Cellular memory in eukaryotic chemotaxis depends on the background chemoattractant concentration

Richa Karmakar,[1] Man-Ho Tang,[1] Haicen Yue,[2] Daniel Lombardo,[1] Aravind Karanam,[1] Brian A. Camley,[3] Alex Groisman,[1] and Wouter-Jan Rappel[1,*]

[1]*Department of Physics, University of California, San Diego, La Jolla, California 92093, USA*
[2]*Courant Institute for Mathematical Sciences, New York University, New York, New York 10012, USA*
[3]*Department of Physics & Astronomy, Department of Biophysics, Johns Hopkins University*

Cells of the social amoeba *Dictyostelium discoideum* migrate to a source of periodic traveling waves of chemoattractant as part of a self-organized aggregation process. An important part of this process is cellular memory, which enables cells to respond to the front of the wave and ignore the downward gradient in the back of the wave. During this aggregation, the background concentration of the chemoattractant gradually rises. In our microfluidic experiments, we exogenously applied periodic waves of chemoattractant with various background levels. We find that increasing background does not make detection of the wave more difficult, as would be naively expected. Instead, we see that the chemotactic efficiency significantly increases for intermediate values of the background concentration but decreases to almost zero for large values in a switch-like manner. These results are consistent with a computational model that contains a bistable memory module, along with a non-adaptive component. Within this model, an intermediate background level helps preserve directed migration by keeping the memory activated, but when the background level is higher, the directional stimulus from the wave is no longer sufficient to activate the bistable memory, suppressing directed migration. These results suggest that raising levels of chemoattractant background may facilitate the self-organized aggregation in *Dictyostelium* colonies.

*Keywords*: *Dictyostelium discoideum*, chemotaxis, cell migration, bistability

## I. INTRODUCTION

Chemotaxis, the movement of cells guided by chemical gradients, plays an important role in many biological processes including tumor dissemination, wound healing, and embryogenesis [1–4]. One of the most studied chemotaxis model organisms is the social amoeba *Dictyostelium discoideum*. Following starvation, *Dictyostelium* cells secrete a chemoattractant, cAMP, in a periodic fashion [5]. This chemoattractant signal is relayed by neighboring cells resulting in waves that sweep over the cell population with periods that range from 6-10 minutes [5–7]. These waves spontaneously organize themselves in spiral or target waves, leading to large-scale patterns of cell migration and eventually generating aggregation centers that attract tens of thousands of cells. Within the resulting aggregates, cells differentiate, with the majority turning into spore cells.

Multiple aspects of this biological system have been investigated using computational and mathematical modeling [8]. Models have addressed instabilities responsible for large scale migration patterns [9, 10], the coupling between intracellular signaling and morphological changes [11–13], and the topology of signaling pathways responsible for guided motion [14–16]. Furthermore, models have addressed potential mechanisms of gradient sensing [8, 17] while a number of studies have examined the role of noise in the chemotactic response [18–20].

Several experimental and modeling studies have also addressed the so-called back-of-the-wave problem in the chemotactic response to traveling waves [21–23]. If cells respond only to spatial gradients, they would move forward in the front and backward in the back of the traveling wave, preventing aggregation. These studies have shown that cells exhibit memory, responding directionally to the front but not the back of the wave, enabling them to move efficiently toward the wave source [22, 23]. For wave periods shorter than 10 min, this memory completely prevented reversals of cell migration, whereas for longer periods, cells started reversing their migration direction in the back of the wave [23]. A mathematical model, consisting of an upstream adaptive module and a downstream bistable module, was able to explain the response of cells to periodic waves of chemoattractant [23]. Similar memory phenomena have also been reported in other biological systems, including chemotactic neutrophils [24, 25].

In the experimental studies of memory in *Dictyostelium* chemotaxis, the cAMP waves were applied exogenously, with the cAMP concentration reaching nearly zero in the troughs of the waves. In cAMP waves that are endogenously produced by starving populations of *Dictyostelium*, however, the background cAMP concentration, $[\mathrm{cAMP}]_{\mathrm{bg}}$,

*Electronic address: rappel@physics.ucsd.edu

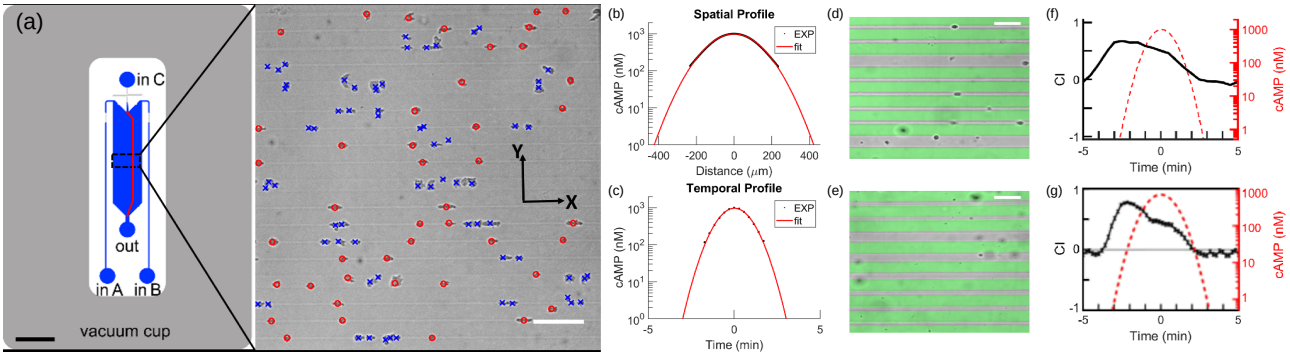


FIG. 1: (a): Left: Schematic of the microfluidic wave device, with observation region indicated by black box (Scale bar: 3 mm). Right: Snapshot of cells moving on the micropatterned substrate, with symbols corresponding to cells identified by the machine learning algorithm (red circles: cells used in our analysis; blue X's: excluded cells that are too close to one another; the blurry spots are out-of-focus dirt particles and other irregularities that are not identified as cells by the machine learning algorithm; scale bar: 100 $\mu$m). (b-c): Spatial (b) and temporal profile (c) of the cAMP wave, determined from the fluorescent intensity of the dye, and the result of the Gaussian fit. (d-e): Images of the two substrate patterns used in this study, with green highlighting the location of the PEG-gel stripes. The pattern consists of either 4 narrow ($\sim 10\mu$m) and 1 wide ($\sim 25\mu$m) untreated stripes (d) or of 6 variable width stripes, ranging from $\sim 6\mu$m to $\sim 25\mu$m (e). In both patterns, the untreated stripes are separated by 30 $\mu m$ wide non-adhesive PEG-gel stripes. Scale bar: 50 $\mu m$. (f-g): The CI as a function of time for the current experiment using a micropatterned substrate (f) and in a previous study [23], using a non-patterned substrate (g). The results are qualitatively similar, indicating that restricting the cells to 1D stripes does not affect their chemotactic behavior.

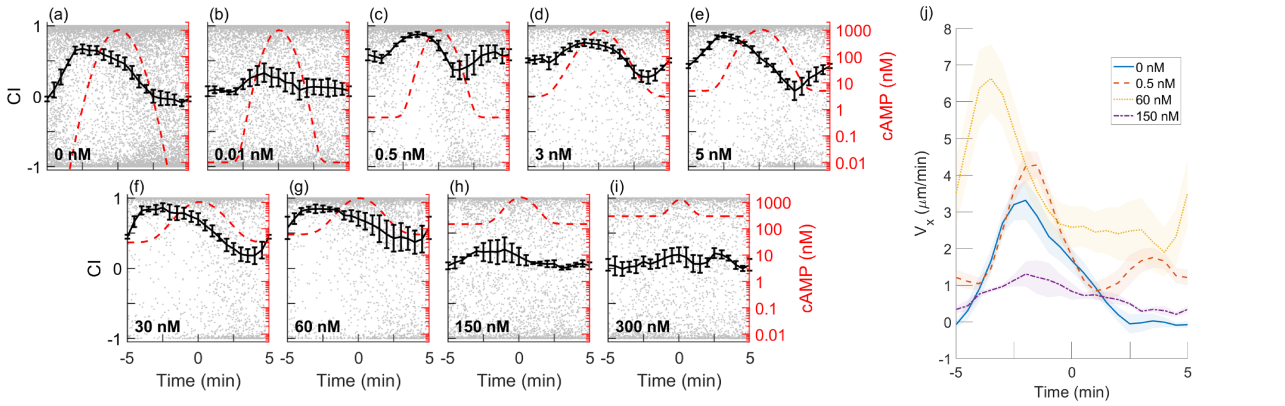


FIG. 2: (a-i) Experimentally determined average CI as a function of time (measured relative to peak of wave) for different concentrations of background cAMP (0-150nM). In each panel, gray dots represent the CI of individual cells, the black curve is the binned average over N=3-4 different experiments, and the dashed red line is the cAMP concentration of the wave. (j) Average x-component of the velocity of cells for different concentrations of background cAMP. Time is binned in intervals of 0.5 min. Error bars in this figure represent the standard error of the mean obtained using bootstrapping.

increases from cycle to cycle [26]. This increase occurs because secreted cAMP is not completely removed by phosphodiesterases (PDEs), enzymes that are responsible for the degradation of cAMP and that are also secreted by the cells [27]. Hence, the question how a non-zero $[\text{cAMP}]_{\text{bg}}$ affects chemotaxis is relevant to the aggregation, sporulation, and survival of *Dictyostelium*. Naively, one would expect a decrease in the cell's ability to migrate towards the source of the wave since the fractional gradient across the cell body, and thus the signal-to-noise ratio, decreases for increasing $[\text{cAMP}]_{\text{bg}}$[28]. Another possibility is that the cells fully adapt to $[\text{cAMP}]_{\text{bg}}$, rendering the ability of cells to respond to gradients independent of the background concentration [29].

To experimentally study this question, we used a modified version of the microfluidics device from Ref. [23] in which a traveling, bell-shaped wave of cAMP with a peak of 1000 nM periodically sweeps across a gradient channel at a constant speed (Fig. 1a; see Appendix A for further details). The fluorescent intensity profile with $[\text{cAMP}]_{\text{bg}}$=0 was well fitted using a Gaussian (Fig. 1b-c and Appendix A) and the resulting wave profile is similar to the one measured

for natural waves of cAMP [30, 31]. Importantly, and in contrast to previous studies, the background concentration of cAMP was a variable parameter. Another major modification was that the glass substrate in the gradient channel was micropatterned with ∼1.5 $\mu$m thick stripes of cell adhesion-blocking polyethylene glycol (PEG) gel. Examples of the two types of micropatterned substrates used in this study are shown in Fig. 1d-e. These substrates limit the adhesion and migration of *Dictyostelium* cells to ∼6-∼25 $\mu$m wide stripes of non-PEG treated glass oriented in the x-direction, along the gradient and perpendicular to the flow. A detailed description of these micropatterned substrates can be found in Ref. [32], where it was shown that cells are nearly exclusively constrained to glass stripes. As a result, cell migration was effectively one-dimensional (1D), either up or down the gradient (positive or negative x-direction), greatly facilitating the collection and analysis of data as compared to 2D chemotaxis on a standard glass substrate.

In our experiments, we exposed cells to repeated waves of cAMP and recorded their movement, excluding the first wave. We used cells of the axenic *Dictyostelium discoideum* strain AX4 that were transformed to express a fusion of GFP to LimE (Δ coil LimE-GFP) and a gene encoding a fusion of RFP to Coronin (LimE GFP/corA RFP) [33]. The cells were grown in submerged shaking culture in HL5 medium (35.5g HL5 powder (Formedium, Norfolk, UK) and 10mL Penicillin-Streptomycin (10,000 U/mL; Gibco, Thermo Fisher Scientific, USA) per liter of DI water) [34]. For starvation, when cells reached their exponential growth phase (3-4 $\times$ $10^6$ cells/mL), they were harvested by centrifugation at 3000 rpm for 5 min, resuspended in $KN_2$/Ca buffer (14.6 mM $KH_2PO_4$, 5.4 mM $Na_2HPO_4$, 100 $\mu$M $CaCl_2$, pH 6.4), collected by centrifugation, and re-suspended in $KN_2$/Ca at $10^7$ cells/mL. Cells were developed for 5 h with pulses of 50 nM cAMP added every 6 min. Differential interference contrast (DIC) images were taken every 15 s in four fields of view spanning the width of the chemotaxis channel, 2800 $\mu$m away from the cAMP inlet, on a spinning-disk confocal Zeiss Axio Observer inverted microscope using a 10X objective and a Roper Cascade QuantEM 512SC camera. Images were captured and analyzed by using Slidebook 6 (Intelligent Imaging Innovations).

Cells were tracked with a custom-made machine-learning algorithm detailed in Appendix B. Only cells that were at least 33 $\mu$m from neighboring cells were used in the analysis (marked by red circles in Fig. 1a) while cells that were part of clusters were not taken into account (marked by blue crosses in Fig. 1a). This algorithm was able to capture more than 90% of single cells, as determined by manual counting. Using cell tracks, we quantified the directional response by computing the chemotactic index CI, defined as ratio between the velocity in the $x$ direction and the speed, computed as the difference in the x-position 3 frames prior and 3 frames forward (a 90 s interval): CI=$V_x$/V. Thus, this quantity ranges from +1 (cells with velocity perfectly aligned to the $+x$ direction), to -1 (cells with velocity perfectly aligned to the $-x$ direction).

## II. EXPERIMENTAL RESULTS

We first examined how cells responded to chemoattractant waves with a period of 10 minutes and very low background concentration; $[\text{cAMP}]_{\text{bg}}$=0 and 0.01 nM). This wave period was chosen since it corresponds to the largest period for which the CI in 2D assays remained positive in the back of the wave [23]. The CI for these background concentrations, shown as a black line in Figs. 2a and b, computed by averaging over different experiments and over 30s time-intervals, was nearly zero for cells ahead of the wave front, steeply increased to a maximum of ∼0.7 as cells were exposed to the wave front, stayed high after the peak of the wave has passed, and gradually decayed to near zero but never became negative. The response for zero background is qualitatively similar to that in 2D *Dictyostelium* chemotaxis assays on plain substrates [23], indicating that constraining the cells to narrow stripes does not change their behavior and that the cellular memory reported in 2D assays is fully manifested in 1D assays as well (Fig. 1f-g).

Next, we exposed cells to the same periodic waves but with larger background concentrations ($[\text{cAMP}]_{\text{bg}}$=0.5, 3, 5, 30, and 60 nM) (Fig. 2c-g). We found that the average CI improved for these values of $[\text{cAMP}]_{\text{bg}}$: the CI remained much greater than 0 during the entire wave cycle. Furthermore, the CI showed a clear minimum after the peak of the wave has passed and *increased* towards the end of the wave cycle even though $[\text{cAMP}]_{\text{bg}}$ was at its lowest level. For the two largest values of $[\text{cAMP}]_{\text{bg}}$ tested, $[\text{cAMP}]_{\text{bg}}$=150 nM and 300 nM, the CI was reduced and remained close to zero throughout the entire wave cycle (Fig. 2h-i). Both the increase in average CI for small values of the background concentration (0.01 to 0.5nM transition) and the decrease in average CI for large values of the background concentration (60 to 150nM transition) were significant ($p < 10^{-4}$, using a z-test). Thus, the background cAMP concentration has a profound effect on the chemotactic response, with intermediate/large values of $[\text{cAMP}]_{\text{bg}}$ enhancing/suppressing the response.

The effect of the background concentration was also evident from the quantification of the x-component of the velocity, $V_x$. This quantification is shown in Fig. 2e where we plot $V_x$, also averaged over different experiments and over 30s time-intervals, as a function of time for different $[\text{cAMP}]_{\text{bg}}$. While this velocity component remained positive or close to zero during the entire cycle for all values of $[\text{cAMP}]_{\text{bg}}$, its maximum value is clearly larger for intermediate values of $[\text{cAMP}]_{\text{bg}}$ than for $[\text{cAMP}]_{\text{bg}}$=0nM. Furthermore, $V_x$ is significantly reduced for the large background concentrations ($[\text{cAMP}]_{\text{bg}}$=150 nM).

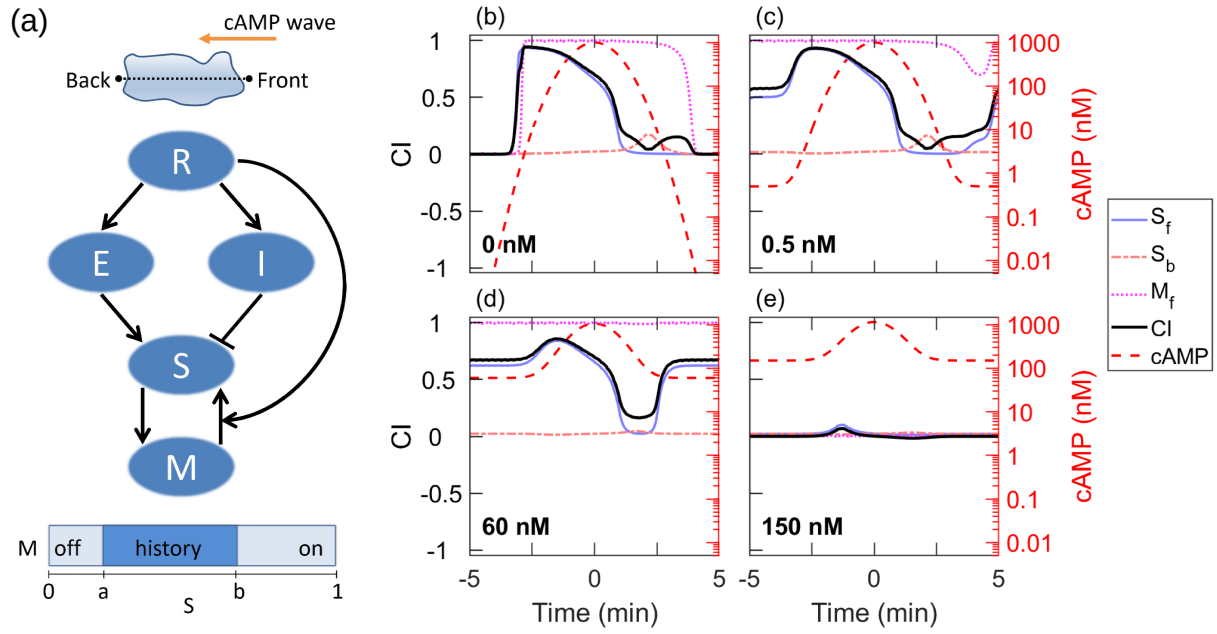


FIG. 3: (a) Schematic diagram of the chemotactic model, consisting of a receptor $R$, an activator $E$, an inhibitor $I$, a response element $S$, and a memory component $M$. Simulations are carried out in a 1D geometry (top drawing). As indicated by the bottom bar, $M$ is bistable, with a low and a high state, determined by parameters a and b. (b-e) Model results for different background cAMP concentrations added to a periodic wave, shown as a dashed red line. The black line represents the CI, the blue (light gray)/red (dash-dotted) line is the response $S$ at the front/back of the cell, and the dotted magenta line corresponds to the memory $M$ at the front.

## III. MODEL RESULTS

To investigate plausible mechanisms for this enhanced cellular memory, we turned to modeling. Specifically, we asked whether the cellular memory model developed by Skoge *et al.* [23] can reproduce the experimental results. This model describes the chemotaxis pathway in terms of abstract variables, although, for some, identification with biochemical components may be possible. Key features of this model are perfect adaptation upon uniform stimulation and cellular memory in gradients [23, 35]. It is schematically shown in Fig. 3a and contains an adaptive module, which incorporates an incoherent feedforward Local Excitation Global Inhibition (LEGI) mechanism [14, 15] and consists of a receptor $R$, an activator $E$, an inhibitor $I$ and a response element $S$ (Fig. 3a). In addition, the model contains a memory module, which is assumed to be bistable such that its component $M$ can be either in a low or high state. The transition between these state is determined by two thresholds, $a$ and $b$ and $M$ feeds back to $S$. Importantly, this feedback depends on $R$ and this non-adaptive link may be thought of as representing parallel pathways for chemotaxis described in experimental studies [36]. For simplicity, we neglect the detailed morphology of the cell and model it as a 10 $\mu$m line with the two endpoints representing the front and back, respectively (Fig. 3a). At the front, the model is written as

$$\frac{dR_f}{dt} = k_R(\mathrm{cAMP} + \mathrm{cAMP_{bg}})(R_f^{tot} - R_f) - k_{-R}R_f \tag{1}$$

$$\frac{dE_f}{dt} = k_E R_f - k_{-E}E_f \tag{2}$$

$$\frac{dM_f}{dt} = -k_{Mem}M_f(M_f - M_f^{tot})\left(M_f - M_f^{tot}\frac{b - s_f}{b - a}\right) \tag{3}$$

$$\frac{dS_f}{dt} = k_S E_f \frac{S_f^{tot} - S_f}{K_{m1} + S_f^{tot} - S_f} - k_{-S} I \frac{S_f}{K_{m2} + S_f} + k_{S2} M_f R_f \frac{S_f^{tot} - S_f}{K_{m3} + S_f^{tot} - S_f} \tag{4}$$

and a similar set of equations applies for the components at the back, labeled with subscript $b$. The first equation describes the binding/unbinding dynamics of cAMP to the receptor with on and off rates $k_R$ and $k_{-R}$, respectively. Here, cAMP is the time-varying concentration due to the wave and its dynamics is taken from a Gaussian fit to the wave profile (Fig. 1b-c). The second equation models the activator dynamics, parametrized by the activation rate

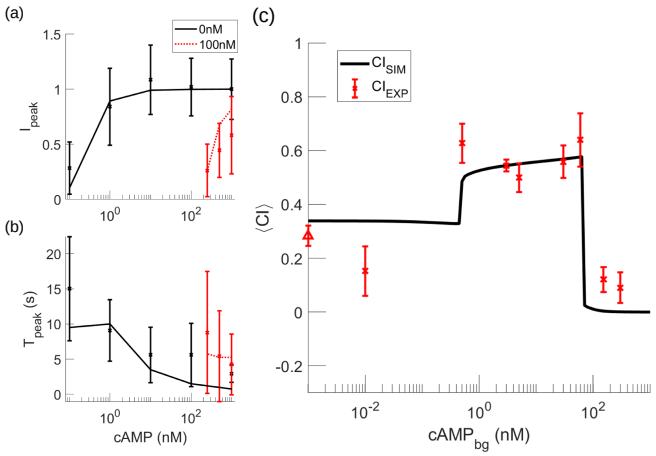


FIG. 4: (a-b): Comparison between experimental results from Ref. [35] (symbols) and model results. Shown are the maximum change in intensity $I_{peak}$ (a) and its corresponding time $T_{peak}$ (b) as a function of the uniform change in cAMP concentration for two different cAMP pretreatment concentrations. (c): Average CI (red symbols) versus background cAMP concentration.

$k_E$ and the degradation rate $k_{-E}$. The third equation describes the bistable memory module, which has two stable steady states 0 and $M_f^{tot}$. The output of the model, $S$, obeys Michaelis-Menten kinetics and is activated with rate $k_S$ by the activator E. It is de-activated with rate $k_{-S}$ by an inhibitor $I$, which diffuses within the interior of the cell. We will assume that $I$ is uniform throughout the cell, corresponding to a high diffusion rate, and is activated by the average of $R$ between the front and the back $R_{av} = (R_f + R_b)/2$, along with a small basal activity $k_{basal}$, and can spontaneously degrade with rate $k_{-I}$:

$$\frac{dI}{dt} = k_I(k_{basal} + R_{av}) - k_{-I}I \tag{5}$$

We set the Michaelis constants, $K_{m1}$ and $K_{m2}$, to be small ($K_{m1}, K_{m2} \ll 1$) to achieve near zero-order ultra-sensitivity, which, consistent with experiments, can result in the amplification of shallow external cAMP gradient [37, 38]. The last term in the equation for $S_f$ describes the feedback from the memory module to the activation of $S_f$, parametrized by the activation rate $k_{S2}$ and Michaelis constant $K_{m3}$. For simplicity, we will take $M_f^{tot} = M_b^{tot} = S_f^{tot} = S_b^{tot} = R_f^{tot} = R_b^{tot} = 1$. The equations were simulated using an adaptive Runge-Kutta method with variable step size. To prevent the memory from becoming trapped in a fixed point, we reset $M_f$ and $M_b$ every t=15s to $\delta$ or $1-\delta$ if their values are smaller than $\delta$ or larger $1-\delta$ ($\delta$=0.01).

Model parameters were determined using a fitting procedure (detailed in Appendix C), which minimized a loss function $L$ that compared simulation results ($x_{sim}$) to experimental results ($x_{exp}$) with uncertainty $\sigma_{exp}$: $L = \sum_{n=1}^{N} |x_{exp} - x_{sim}|/(N\sigma_{exp})$. Here, $N = 56$ with 46 data points chosen from previous experiments using different microfluidic devices [23, 35] and the remaining 10 data points chosen from the current experiments. Details of the previous data points used in the fitting are presented in Appendix C while the new data points consisted of data for $[\text{cAMP}]_{\text{bg}}$ of 0, 0.01, 0.5, 60, and 150nM that were chosen since they represent the three qualitatively distinct responses observed in the experiments. Specifically, in our fitting we required that $M_f$ 2.5 minutes before and 5 minutes after the peak to be either 0, corresponding to a small experimental value of CI, or 1, corresponding to a high CI in the experiments. Simulated annealing was used to find possible global minima, followed by a pattern search to obtain the local minima using the Matlab routine patternsearch. Importantly, the parameter values for the bistable and adaptive module were taken from previous studies [23, 35] and only parameters associated with the memory module ($a$, $b$, $k_{Mem}$, $k_{S2}$ and $K_{m3}$) were adjusted. The parameter values obtained by our fitting procedure are listed in Table 1 while a fit to previous data is shown in Fig. 4a-b.

Simulation results for $[\text{cAMP}]_{\text{bg}}$=0 (Fig. 3b) show that the chemotactic response, quantified by CI (computed, following our earlier study [23], as a linear combination of $S$ and $M$: CI= $0.1831(M_f - M_b) + 0.8169(S_f - S_b)$ is in qualitative agreement with the experimentally measured CI (cf. Fig. 2a). In this case, as the wave approaches the cell, the small difference in cAMP between the front and back is greatly amplified because of the ultra-sensitivity of the response. The resulting large increase in $S_f$ (blue (light gray) line) causes a transition of $M_f$ (dotted magenta line) to the high state. Since $S_b$ (dash-dotted red line) remains low, $M_b$ stays in the low state, and the CI is high (black line). After the wave sweeps over the cell, $S_f$ decreases while $M_f$ remains high for several minutes, resulting in cellular memory and an elevated CI. Eventually, however, the low values of $S_f$ cause a transition of $M_f$ to its low state and the CI decreases to zero (see below and Fig. 5).

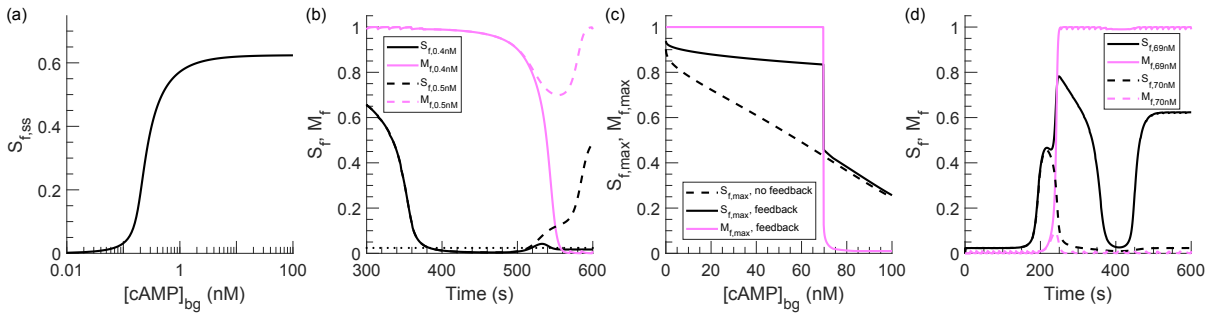


FIG. 5: A: Steady-state value of $S_f$ as a function of uniform [cAMP]$_{bg}$ for the case $M_f$=1. B: $S_f$ and $M_f$ as a function of time in the full model for a value of [cAMP]$_{bg}$ that does ([cAMP]$_{bg}$=0.5nM; dashed lines) and does not ([cAMP]$_{bg}$=0.4nM; solid lines) result in persistent memory. C: Maximum value of $S_f$ and $M_f$ in a wave as a function of [cAMP]$_{bg}$. There is a sharp, switch-like transition at [cAMP]$_{bg}$≈69nM. D: Response of the full model for [cAMP]$_{bg}$ just below ([cAMP]$_{bg}$=69nM; solid lines) and just above ([cAMP]$_{bg}$=70nM; dashed lines) the switch-like transition.

Intermediate values of [cAMP]$_{bg}$ ([cAMP]$_{bg}$=0.5-69 nM) result in higher values of $S_f$, maintaining $M_f$ in a high state for the entire wave period (Fig. 3c-d). This increase in $S_f$ is due to the feedback from $M_f$ to $S_f$, which is, through the non-adaptive link, proportional to the receptor occupancy $R_f$. Since this occupancy is an increasing function of [cAMP]$_{bg}$, the feedback loop between $S_f$ and $M_f$ contributes to a sustained positive CI throughout the entire wave cycle (Fig. 3c-d), in agreement with the experimental results. This feedback from high $M_f$ is also responsible for the increase of $S_f$ in the back of the wave (Fig. 3c-d). As a result, the CI shows a distinct increase near the end of a cycle, which is, again, consistent with the experimental results.

For [cAMP]$_{bg}$>69 nM, both $S_f$ and CI remain close to 0 during the entire cycle, which is consistent with the experimental results for [cAMP]$_{bg}$=150 and 300 nM. The reason for this is that the amplification of $S_f$ due to the ultra-sensitivity of the response is reduced for increased values of [cAMP]$_{bg}$ (see below and Fig. 5). As a result, the value of $S_f$ is not sufficiently large to bring $M_f$ to its high state. Consequently, $M_f$ remains in the low state, leading to a short and weak response of $S_f$ and an overall low CI (Fig. 3e). Note that for our parameter values, the dissociation constant for the receptors is $K_d \approx 408$nM. Thus, the absence of a strong chemotactic response for high values of [cAMP]$_{bg}$ is not due to receptor saturation but is directly linked to the bistability and the ultra-sensitivity of the pathway.

We also used the modeling results to compute the chemotactic index averaged in time over the entire wave cycle, ⟨CI⟩. The dependence of ⟨CI⟩ on [cAMP]$_{bg}$ has three distinct regimes (Fig. 4c). For very small values of [cAMP]$_{bg}$ ([cAMP]$_{bg}$< 0.5 nM) ⟨CI⟩ remains close to its value at [cAMP]$_{bg}$=0. For these values of [cAMP]$_{bg}$, the memory is only turned on during part of the wave cycle. In contrast, for intermediate values of [cAMP]$_{bg}$ (0.5 nM ≤ [cAMP]$_{bg}$ ≤ 69 nM), $M_f$ is in the high state during the entire cycle, resulting in a nearly constant and high ⟨CI⟩. Finally, for [cAMP]$_{bg}$ > 69 nM, $M_f$ is always in the low state and ⟨CI⟩ is close to 0. Notably, due to the bistable dynamics of our memory module, the transitions between these regimes are very abrupt and switch-like. To determine whether our experimental data also exhibited this switch-like behavior, we computed the average CI in the experiments. The results are plotted as symbols in Fig. 4c and are close to the results of the model (line). Most importantly, ⟨CI⟩ decreases in a switch-like fashion from as much as ∼0.6 at [cAMP]$_{bg}$=60nM to as little as ∼0.1 at [cAMP]$_{bg}$=150nM, in agreement with the bistable dynamics of the memory module.

To understand the transition in the model behavior for small values of [cAMP]$_{bg}$, shown in Fig. 4c, it is useful to examine the response of $S_f$ with $M_f = 1$. For this case, we plot in Fig. 5a the steady state solution for $S_f$ as a function of uniform [cAMP]$_{bg}$(i.e., in the absence of a wave). $S_f$ increases from 0 to approximately 0.6 as the background cAMP concentration increases. This increase is due to the feedback from $M_f$ to $S_f$, which is proportional to the receptor occupancy $R_f$, an increasing function of [cAMP]$_{bg}$. The dependence of $S_f$ on [cAMP]$_{bg}$ explains why for small values of [cAMP]$_{bg}$ the chemotactic index CI reduces to zero following the wave (see Fig. 3a and Fig. 4c). This is further illustrated in Fig. 5b where we plot $S_f$ and $M_f$ for [cAMP]$_{bg}$=0.4nM and [cAMP]$_{bg}$=0.5nM. For [cAMP]$_{bg}$=0.4nM, $S_f$ remains close to the lower threshold of the bi-stable module (indicated by the dotted line), which causes $M_f$ to transition from the high to the low state, resulting in a vanishing CI. For [cAMP]$_{bg}$=0.5nM, however, the feedback from $M_f$ results in higher values of $S_f$ such that the memory stays in its high state.

To analyze the switch-like behavior of Fig. 5, we can compute the maximum value of $S_f$ in a wave as a function of [cAMP]$_{bg}$. The result is plotted in Fig. 5c, both for the full model (solid line) and for the case without feedback from $M_f$, i.e. $k_{S2} = 0$ (dashed line). As a result of the ultra-sensitivity of the equation, the asymmetry in the response of $S$ is much larger than the asymmetry in the external gradient and the receptor occupancy. As is evident from the

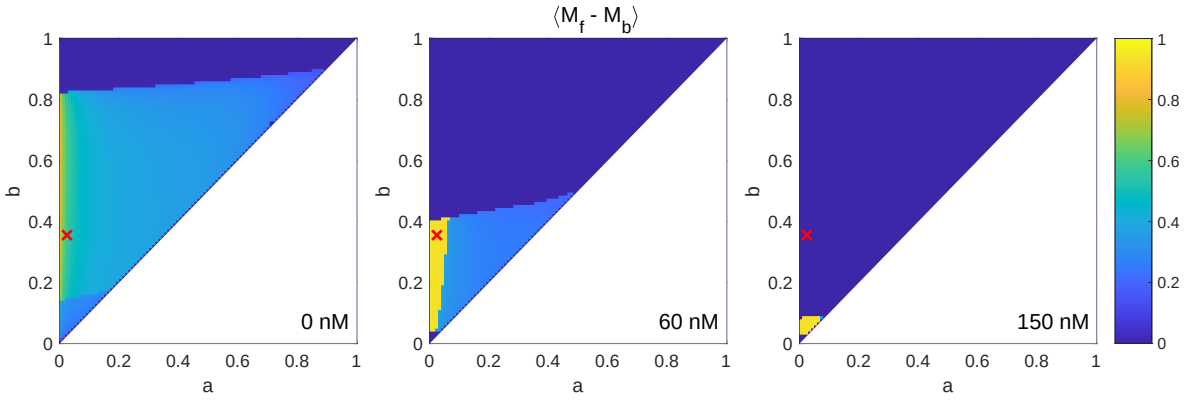


FIG. 6: Phase diagram in the $a-b$ space quantifying $\langle M_f - M_b\rangle$ for three different values of $[\text{cAMP}]_{\text{bg}}$. Three regions, with sharp transitions, can be identified: $\langle M_f - M_b\rangle = 1$ (yellow regions) for which the front memory is always high while the back memory is always low, $\langle M_f - M_b\rangle = 0$ (dark blue regions) corresponding to low memory at the front and the back, and intermediate values of $\langle M_f - M_b\rangle$ for which the front memory is high during part of the wave. The values of $a$ and $b$ corresponding to our study are marked by a red X.

plot, this amplification of $S_f$ is a decreasing function of $[\text{cAMP}]_{\text{bg}}$. Therefore, above a critical value of $[\text{cAMP}]_{\text{bg}}$, $S_f$ is no longer able to cause a transition of $M_f$ from the low to the high state. For the values of $[\text{cAMP}]_{\text{bg}}$ above the critical value, the CI will thus remain low (see Fig. 4). Furthermore, due to the bi-stability of the memory module, $M_f$ exhibits a switch-like transition at a critical value of $[\text{cAMP}]_{\text{bg}}$ (magenta (light gray) line). This is also shown in Fig. 5d where we plot the response of the full model for a value of $[\text{cAMP}]_{\text{bg}}$ just below and just above the critical value. For $[\text{cAMP}]_{\text{bg}}$=70nM, above the critical value, $M_f$ does not transition to the high state and $S_f$ remains close to 0 for the second half of the wave. For $[\text{cAMP}]_{\text{bg}}$=69nM, on the other hand, $M_f$ switches from its low to its high state, which leads to an increased response. After the wave passes, $S_f$ decreases but then increases to $\approx$0.6 due to the persistent memory at the front.

The switch-like transitions are also clearly visible when examining the phase diagram of the response of the model in the $a$-$b$ parameter plane (corresponding to the two thresholds in the memory module). Here, we plot the time averaged difference between the memory at the front and back of the cell, $\langle M_f - M_b\rangle$, for different values of $a$ and $b$ using a color scale (Fig. 6). Since we take $a \leq b$ we only present one-half of the space. The parameter values corresponding to Table 1 and used in our study are indicated by the symbol. For $[\text{cAMP}]_{\text{bg}}$=0nM (left panel), the sharp transitions between three different regions are clearly visible. In the dark blue regions, corresponding to large values of $b$, neither the front nor the back memory is activated, resulting in $\langle M_f - M_b\rangle = 0$. For intermediate values of $b$ and small values of $a$, the memory at the front is permanently activated while $M_b = 0$, which results in $\langle M_f - M_b\rangle = 1$ (yellow region). In the other regions, the front memory is activated only during part of the wave, giving rise to values of $\langle M_f - M_b\rangle$ that are between 0 and 1. Note that our parameters fall within this region of the phase space. For $[\text{cAMP}]_{\text{bg}}$=60nM, the sharp boundary of the yellow region has moved to larger values of $a$, such that our parameter values now fall within the region in which $\langle M_f - M_b\rangle = 1$ (middle panel). Finally, for $[\text{cAMP}]_{\text{bg}}$=150nM, the yellow region has almost completely disappeared and nearly the entire phase diagram, including our parameter set, correspond to $\langle M_f - M_b\rangle = 0$.

## IV. SUMMARY

In summary, we find that the background concentration of the chemoattractant, $[\text{cAMP}]_{\text{bg}}$, has a profound effect on the cellular memory of chemotaxing *Dictyostelium* cells. For intermediate values of $[\text{cAMP}]_{\text{bg}}$ this memory is greatly enhanced, leading to substantially more efficient chemotaxis under periodic waves of cAMP. It is worth noting that the experimentally estimated value of $[\text{cAMP}]_{\text{bg}}$ during the natural aggregation process of *Dictyostelium* cells is $\sim$10nM [26]. This value is within the intermediate range, suggesting that aggregation may be facilitated by increased cellular memory due to accumulating cAMP. For larger values of $[\text{cAMP}]_{\text{bg}}$, the chemotactic response and cellular memory are suppressed. Our experimental results, and in particular the switch-like behavior of the average CI, are fully consistent with our mathematical model. Crucial elements of this model are a bistable memory module, which allows cells to ignore the back of the wave, an ultra-sensitive response, responsible for the amplification of the chemoattractant gradient, and a direct, non-adaptive link between input signal and response, which explains the long-lasting memory

for intermediate values of $[\text{cAMP}]_{\text{bg}}$. Future work will be required to identify the precise biochemical components that are responsible for the observed behavior.

## V. ACKNOWLEDGMENTS

R.K. and M-H.T. contributed equally to this work. We acknowledge support from by the National Science Foundation under grant NSF PHY-1915491 (BC), PHY-1411313 (AG), and PHY-1707637 (W.-J.R.).

## VI. APPENDIX

### A. Microfluidic device, device preparation, and experimental setup

The microfluidic system produces bell-shaped pulses of concentration that periodically sweep over cells on the substrate, thus emulating the spatial and temporal pattern of concentration in a periodic traveling wave. The microfluidic system is comprised of a microfluidic device and a flow-driving setup, which are modified versions of the device and setup described in our previous publication [23]. The microfluidic device consists of a micromachined polydimethylsiloxane (PDMS) chip and a #1.5 microscope cover glass substrate with a periodic micropattern of stripes of polyethylene glycol (PEG) gel. The PEG-gel stripes are all $\sim$1.5 $\mu$m high and $\sim$30 $\mu$m wide and one of two substrate patterns are used: 1) one 25 $\mu$m wide glass (non-treated) stripe for every four 10 $\mu$m wide glass stripes or 2) variable width stripes, repeated every 6 stripes, ranging from $\sim 6\mu$m to $\sim 25\mu$m (Fig. 1d-e). We have verified that our results are independent of the stripe width. Because developed *Dictyostelium* cells cannot adhere to the surface of PEG-gel, adherent *Dictyostelium* cells are confined to glass stripes, making their migration along the 10 $\mu$m wide glass stripes nearly one-dimensional (1D) [32].

The microfluidic device has three inlets (A-C) and one outlet (see Fig. 1). Its main functional area is an $\sim$100 $\mu$m deep chemotaxis channel with a width of 2200 $\mu$m and an $\sim$7 mm long rectilinear part. At the entrance of the chemotaxis channel, a $\sim$200 $\mu$m wide stream of a concentrated solution of cAMP (coming from inlet C) is squeezed (hydrodynamically focused) between two streams of plain buffer or of cAMP solutions with a lower concentration (coming from the inlets A and B), which together fill the rest of the 2200 $\mu$m wide chemotaxis channel. As the focused stream of cAMP advances down the chemotaxis channel (along the y-axis), the diffusion of cAMP molecules across the boundaries of the stream gradually changes the lateral (across the flow, x-axis) profile of cAMP from its initial rectangular shape to a bell-shaped curve. At the standard experimental conditions, [cAMP] in the concentrated solution is 1400 nM, the mean flow velocity in the gradient channel is $\sim$300 $\mu$m/s, and the chemotaxis is observed $\sim$3 mm downstream from the gradient channel entrance, where the maximal [cAMP] is reduced to $\sim$1000 nM, and the effective width of the stream of concentrated cAMP (full width at half height) is increased to $\sim$230 $\mu$m, both due to diffusion of cAMP across the stream [23]. The microfluidic system operates in a cyclic fashion. In the beginning of a cycle, the volumetric flow rate of the stream of buffer (or low-concentration cAMP solution) from inlet B to the right of the cAMP stream is low, and the volumetric rate of flow of buffer from inlet B to the left of the cAMP stream is high, thus placing the cAMP stream close to the right wall of the gradient channel. The flow rate of the buffer stream on the right linearly increases with time, while the flow rate of the buffer on the left linearly decreases with time, with the total flow rate remaining nearly unchanged. As a result, the high concentration cAMP stream (which is squeezed between the buffer streams) linearly drifts from right to left, and, at a given y-axis position, a bell-shaped pulse of cAMP is sweeping from right to left (in the negative x-axis direction) at a constant speed. The length of the sweep is l$\approx$1425 $\mu$m that for a duration of the sweep T=10 min results in a speed of 2.5 $\mu$m/s for the motion of the cAMP pulse across the gradient channel (note that it takes 30s for the wave to be reset, such that the effective duration is 570s). At the end of a sweep, the flow of the concentrated cAMP solution is turned off, making the concentrated cAMP to completely disappear from the gradient channel, and then the flow rates from inlets A and B restored to their initial values. After that, the flow of the concentrated cAMP solution is turned on again, making the stream of concentrated cAMP reappear at its initial location close to the right wall of the gradient channel, and the next cycle begins. Importantly, the cAMP stream is effectively moved from its final to initial location without directing it (even transiently) anywhere else in the chemotaxis channel. Also, because of the relatively large length of the sweep, and fast decay of [cAMP] with the distance from the peak of the bell-shaped profile, there is $\sim$500 $\mu$m wide region near the middle of the gradient channel, where [cAMP] is very close to the background concentration, both in the beginning and end of each cycle. As a result, all cells in this region are exposed to the same periodically repeating spatiotemporal pattern of [cAMP] and can be pooled and analyzed together, after accounting for a time difference within a cycle of $\Delta t = \Delta x/v_x$, where $\Delta x$ is the distance between cells along the x-axis. Therefore, large sets of data

on chemotactic indices (CIs) and velocities of individual cells at different time points (phases) of the repeated cAMP wave cycle can be collected.

Further details on the operation of the microfluidic device and flow setup and on the experimental procedure as well as a detailed mathematical analysis are provided in SI of Ref. [23]. The following modifications were made to the original experimental setup and procedure of Ref. [23]. (1) Because flow in the microfluidic device is driven and controlled by applying differential pressures between the inlets and the outlets, it is necessary to have substantial fluidic resistances between the inlets and the outlet. In the original device, those resistances were implemented in 100 $\mu$m deep and 60 $\mu$m wide channels, making the device easy to fabricate (all channels had the same depth), but requiring the resistance channel lines to be long, because of their relatively low fluidic resistance per unit length. In the present device, the resistance lines are $\sim$30 $\mu$m deep and $\sim$30 $\mu$m wide channels, which have an $\sim$40 larger fluidic resistance per unit length, greatly reducing the footprint of the microchannel network (at the expense of making the fabrication of the device somewhat more involved). (2) The reduced footprint of the microchannel network makes it possible to seal the PDMS chip against the coverglass with the micropattern of PEG-gel stripes using the application of vacuum ($\sim$ -30 kPa) to a deep (100 $\mu$m) and wide (4 - 6.5 mm) O-shaped grove around the microchannel network that acts as a vacuum cup. This vacuum-assisted sealing is essential, because it allows keeping the micropatterned substrate wet at all times, thus preserving the structure and functionality of the PEG-gel stripes (that *Dictyostelium* cells cannot adhere to). (3) The possibility of attaching the microfluidic chip to a wet substrate also enables direct plating of *Dictyostelium* cells onto the substrate. The PDMS chip is attached to the substrate only after cells settle and adhere to glass stripes. As a result, cell plating is substantially simplified and streamlined as compared with the original microfluidic device, where cells needed to be delivered to the gradient channel through a dedicated inlet and connecting microchannel that are both absent in the present device.

Microfluidic chips were cast in polydimethylsiloxane (PDMS, Sylgard 184 by Dow corning) using a microfabricated master mold, a 5 inch silicon wafer with a micro-relief of UV-curable SU8 photoresist (by MicroChem) produced with UV photolithography [32]. First, an $\sim$30 $\mu$m thick layer of SU8 2015 photoresists was spin-coated onto the wafer, pre-backed, exposed to collimated UV-light through a photomask, and post-baked. Next, the wafer was spin-coated with SU8 2050 photoresist to a total thickness of 100 $\mu$m, pre-baked, exposed to UV-light through a second photomask, post-baked, and developed, revealing a micro-relief with 30 $\mu$m and 100 $\mu$m tall micro-ridges. The 30 $\mu$m deep micro-grooves on the PDMS replica of the mold produced the 30$\times$30 $\mu$m resistance channels, and 100 $\mu$m deep micro-grooves produced all other flow channels and the O-shaped vacuum cups. The PDMS cast was cut into individual chips, and the inlet and outlet holes in the chips were punched with a Luer stub.

To verify the wave profile computed from numerical simulations of the diffusion process [23], we added Alexa Fluor$^{\mathrm{TM}}$ 594 Hydrazide (Invitrogen), a fluorescent dye, to the cAMP solution. The fluorescent intensity profile with $[\mathrm{cAMP}]_{\mathrm{bg}}$=0 was well fitted using a Gaussian

$$\mathrm{cAMP}_{\mathrm{Gauss}}(x) = Ae^{\frac{-(x-x_0)^2}{2\sigma^2}}$$

where the wave peak position was given by $x_0$, the wave width was given by $\sigma$ and its amplitude by $A$. Using the numerical simulations, this amplitude was determined to be 1000 nM at the experimental field of view [23]. An example of a fit is given in Fig. 1b-c. From these fits, we determined $\sigma = 115$ $\mu$m, corresponding to a full width at half maximum of 230 $\mu$m. Furthermore, by using a linear fit to $x_0$ as a function of time, we verified that the wave speed is $v = 2.5$ $\mu$m/s. For non-zero $[\mathrm{cAMP}]_{\mathrm{bg}}$ the cAMP concentration was the Gaussian profile plus a constant equal to the value of $[\mathrm{cAMP}]_{\mathrm{bg}}$ such that the total cAMP profile is given by $\mathrm{cAMP}(x) = \mathrm{cAMP}_{\mathrm{Gauss}}(x) + \mathrm{cAMP}_{\mathrm{bg}}$ .

### B. Cell tracking

A machine learning (ML) model was developed for reliably tracking the complex movement of the *Dictyostelium* cells. 20 videos of cells moving in response to chemical gradients were provided for training of the model. In order to avoid having too many repeated or similar images, only one in every thirty frames was used for training and validating the model, resulting in 140 images. Each of the images, of size 256x256 pixels representing 25% of the full field of view, was assumed to be completely independent. Images were converted to grayscale and normalized. The model used was a U-Net convolutional neural network, which can be trained on very few images and outperforms most existing methods [39]. The model consisted of three rounds of convolution and max pooling, followed by a fully connected layer with 512 elements, and finally three rounds of convolution and upsampling. The convolution layers were 3x3 with 32, 64, and 128 filters. Rectified linear unit (Relu) activation was applied after each convolution. The pooling and upsampling layers were 2x2. Data augmentation, including shifting and flipping of the images, was used during model training to increase the size of the dataset. A labeled dataset was obtained by marking the centroid of cells in a small number of images using human input. A U-Net model was then trained on this small sample and then used

to aid in marking further images. This process was repeated several times until the entire dataset was marked. The labeled dataset was then split with 80% of all images used for training, and 20% used for validation set. In order to avoid target leakage, the model's parameters and hyperparameters were reset and trained only on the new training dataset. Data augmentation was again used to increase the size of the training dataset. The final model consistently tracked 90% of all cells in the validation dataset. Finally, the model was tested on a new set of videos not seen in the original dataset. A comparison between blinded, manual marking of cells and the ML algorithm showed that approximately 97% of cells were tracked by the automated procedure (5623 vs. 5487).

Once cell positions were determined, we computed cell trajectories by connecting nearest points in consecutive frames. Only cells that were within a 300 $\mu$m wide region at the middle of the gradient channel were considered. These cells experienced a full cAMP wave, starting and ending at the background concentration. Furthermore, we only included cells that were continuously recognized for more than 3.5 min, that were moving with an average speed of at least 0.16 $\mu$m/min, and that were at least 33 $\mu$m from the neighboring cells (these cells are marked by red circles in Fig. 1). In addition, although rarely observed, cells moving on the PEG-gel stripes were also excluded. Data from the first cAMP wave was excluded to eliminate any initial differences in cells.

The cell's velocity in the x-direction for a given frame, $V_x$, was computed as the difference in the x-position 3 frames prior and 3 frames after the given frame, divided by the time interval between these frames (90s). The time with respect to the passage of the cAMP peak (phase) was assigned by measuring the distance of the cell from the location of the peak of the wave relative to the extent of the sweep. The CI as a function of time was computed by averaging data points in equally spaced bins of width 0.5 min. The time averaged CI, $\langle \mathrm{CI} \rangle$, was computed by averaging CI in time over the entire wave cycle. The time average of $V_x$, $\langle V_x \rangle$, was calculated in a similar fashion. Experiments were repeated at least three times for each $[\mathrm{cAMP}]_{\mathrm{bg}}$. For each $[\mathrm{cAMP}]_{\mathrm{bg}}$, a distribution (N = 10,000 trials) of sample mean was generated by bootstrapping over the replicate experiments, and the experimental averages and error bars reported in this study were the mean and standard deviation of this resampled distribution.

### C. Parameter fitting

As mentioned in the main text, we minimize the loss function $L = \sum_{n=1}^{N} |x_{exp} - x_{sim}|/(N\sigma_{exp})$ to find the optimal parameters. This loss function compares N=54 experimental data points to simulation data (see main text). We take 46 discrete points from previous experimental data (detailed in Ref. [23]) and 8 points derived from the current study. As in Ref. [23], $\sigma_{exp}$ was taken as the standard deviation of the experimental data or 50% of $x_{exp}$ where standard deviations were not available.

Following Ref. [23], the 46 data points using previous studies were chosen as follows: 24 data points were taken from uniform dose response data where cells were exposed to uniform stimulus switching from 0nM or 100nM to higher concentrations [35]. The peak amplitudes, peak times and the state of memory module $M$ were fitted (see also Fig. 4a-b). Additionally, 15 data points were chosen from gradient-to-uniform data obtained from experiments in which cells were first exposed to a gradient (0-100 nM across a 70 $\mu$m wide channel), followed by a uniform concentration of 0, 1, 10, 20 or 50nM [23]. These experiments, detailed in Ref. [23], quantified the localization of activated Ras, a directional sensing marker, using the Ras-binding domain of Raf tagged to GFP (RBD-GFP). The times for disappearance and reappearance as well as the ratios of fluorescence intensity before and after the switching from gradient to uniform concentration were fitted. As indicated from the experiments, we required the memory $M_f$ to stay high (i.e., $M_f$=1) for a uniform concentration of 10, 20 and 50nM and to become low ($M_f$=0) for 0nM . The final 7 data points were chosen from gradient reversal data where the initial gradient was switched to a reversed

| Parameter | Value | Parameter | Value |
|---|---|---|---|
| $k_R$ | 0.002463 $nM^{-1} \cdot s^{-1}$ | $k_{-R}$ | 1.006 $s^{-1}$ |
| $k_E$ | 0.159 $s^{-1}$ | $k_{-E}$ | 0.159 $s^{-1}$ |
| $k_I$ | 0.139 $s^{-1}$ | $k_{-I}$ | 0.139 $s^{-1}$ |
| $k_{basal}$ | 0.000015 $nM$ | $k_{Mem}$ | 0.2550 $nM^{-2} \cdot s^{-1}$ |
| $a$ | 0.0239 $nM$ | $b$ | 0.3550 $nM$ |
| $k_S$ | 2000 $s^{-1}$ | $K_{m1}$ | 0.018 $nM$ |
| $k_{-S}$ | 2048 $s^{-1}$ | $K_{m2}$ | 0.001 $nM$ |
| $k_{S2}$ | 149.4 $s^{-1}$ | $K_{m3}$ | 0.0366 $nM$ |
| $M_f^{tot}$ | 1 | $M_b^{tot}$ | 1 |
| $R_f^{tot}$ | 1 | $R_b^{tot}$ | 1 |
| $S_f^{tot}$ | 1 | $S_b^{tot}$ | 1 |

TABLE I: Model parameters.

gradient of 100-0nM, 75-25nM or 60-40nM across the gradient chamber. The ratios of fluorescent RBD-GFP intensity before and after the switching were fitted. The memory was required to reverse in the 100 to 0nM profile and remain unchanged in the 60 to 40nM profile. Further details of these data points can be found in Ref. [23].

The "new" 10 data points were chosen from the current background experiments with $[\text{cAMP}]_{\text{bg}}$= 0, 0.01, 0.5, 60 and 150nM. To match with the experimental results, which showed that cells have a high CI during the front of the wave for $[\text{cAMP}]_{\text{bg}}$= 0 and 0.01 nM, persistent high CI for $[\text{cAMP}]_{\text{bg}}$=0.5 and 60 nM, and significantly reduced CI for $[\text{cAMP}]_{\text{bg}}$=150nM, we required the front memory, $M_f$, at 2.5 minutes before the peak of the wave, when cells experienced a positive gradient, to be high for $[\text{cAMP}]_{\text{bg}}$=0, 0.01, 0.5 and 60nM and low for 150nM. At 5 minutes after the peak, at a near-zero cAMP concentration, $M_f$ was required to be low for $[\text{cAMP}]_{\text{bg}}$=0, 0.01 and 150nM and high for $[\text{cAMP}]_{\text{bg}}$=0.5 and 60nM.

We fitted the five parameters ($a$, $b$, $k_{Mem}$, $k_{S2}$ and $Km_3$) related to the memory module using the lower bound constraints of [0.001, 0.001, 0.005, 20, 0.0001] and upper bound constraints of [1, 1, 5, 200000, 1] in units of [nM, nM, $\text{nM}^{-2}\text{s}^{-1}$, $\text{s}^{-1}$, nM]. To minimize $L$ we used simulated annealing, which avoids trapping in local minima of the parameter space, and uses an artificial temperature that is decreased during the parameter search such that sampling becomes more and more selective. In each iteration, a new parameter set was generated from the previous one with a step size based on this artificial temperature. The difference in the value of the loss function between the new and previous iteration was then computed. For a negative difference the new parameter set was automatically accepted while for a positive difference the new parameter set was accepted with a chance that ranged between 0 to 50% and which was based on the loss function difference and the artificial temperature. The search was carried out in log space to cover the wide range of parameter values and the algorithm was concluded when the difference in loss function became smaller than 0.01 for more than 500 iterations. Multiple runs of simulated annealing were conducted with randomized initial parameter values. At the end of each run, pattern search was applied to obtain more precise local minima, using Matlab routine patternsearch. In each iteration, this algorithm attempts parameters values at a fixed step from the previous parameters. If the loss function was reduced, the step size would be doubled in order to explore a wider space. If the loss function did not reduce, the step size would be halved. The parameter search terminated when both the change in loss function became smaller than 0.01 and the absolute step size became smaller than 0.0001 in log10 space.

The final parameters are listed in Table 1 and correspond to $L = 0.556$. As in Ref. [23] (Fig. S5b in that study), we can compare the simulation results with experimental results of Takeda *et al.*, which recorded the intensity of RBD-GFP following a sudden change in uniform cAMP concentration [35]. In Fig. 4a-b, we plot the numerically computed intensity peak, $I_{peak}$, and the time corresponding to the maximum peak amplitude, $T_{peak}$ as lines. These results are in good agreement with the experimental results, plotted as symbols. When we consider the loss function $L'$ that includes only the 46 data points from the previous experiments, the current parameter set gives $L' = 0.655$ while the original parameter set results in $L' = 0.731$.


[1] Evanthia T Roussos, John S Condeelis, and Antonia Patsialou. Chemotaxis in cancer. *Nature Reviews Cancer*, 11(8):573, 2011.

[2] Marco Baggiolini. Chemokines and leukocyte traffic. *Nature*, 392(6676):565, 1998.

[3] Anne J Ridley, Martin A Schwartz, Keith Burridge, Richard A Firtel, Mark H Ginsberg, Gary Borisy, J Thomas Parsons, and Alan Rick Horwitz. Cell migration: integrating signals from front to back. *Science*, 302(5651):1704–1709, 2003.

[4] Denise J Montell. Border-cell migration: the race is on. *Nature Reviews Molecular Cell Biology*, 4(1):13–24, 2003.

[5] Thomas Gregor, Koichi Fujimoto, Noritaka Masaki, and Satoshi Sawai. The onset of collective behavior in social amoebae. *Science*, 328(5981):1021–1025, 2010.

[6] W Roos, V Nanjundiah, D Malchow, and G Gerisch. Amplification of cyclic-AMP signals in aggregating cells of dictyostelium discoideum. *FEBS letters*, 53(2):139–142, 1975.

[7] BM Shaffer. Secretion of cyclic AMP induced by cyclic AMP in the cellular slime mould Dictyostelium discoideum. *Nature*, 255(5509):549, 1975.

[8] Herbert Levine and Wouter-Jan Rappel. The physics of eukaryotic chemotaxis. *Phys Today*, 66(2), Feb 2013.

[9] Herbert Levine, Igor Aranson, Lev Tsimring, and Thai Viet Truong. Positive genetic feedback governs cAMP spiral wave formation in dictyostelium. *Proceedings of the National Academy of Sciences*, 93(13):6382–6386, 1996.

[10] Giovanna De Palo, Darvin Yi, and Robert G Endres. A critical-like collective state leads to long-range cell communication in Dictyostelium discoideum aggregation. *PLoS biology*, 15(4), 2017.

[11] Danying Shao, Wouter-Jan Rappel, and Herbert Levine. Computational model for cell morphodynamics. *Phys Rev Lett*, 105:108104, 2010.

[12] Danying Shao, Herbert Levine, and Wouter-Jan Rappel. Coupling actin flow, adhesion, and morphology in a computational cell motility model. *Proc Natl Acad Sci U S A*, 109(18):6851–6856, 2012.

[13] Wieland Marth and Axel Voigt. Signaling networks and cell motility: a computational approach using a phase field description. *Journal of mathematical biology*, 69(1):91–112, 2014.

[14] Carole A Parent and Peter N Devreotes. A cell's sense of direction. *Science*, 284(5415):765–770, 1999.

[15] Andre Levchenko and Pablo A. Iglesias. Models of eukaryotic gradient sensing: application to chemotaxis of amoebae and neutrophils. *Biophys J*, 82:50–63, 2002.

[16] Wouter-Jan Rappel and Herbert Levine. Receptor noise limitations on chemotactic sensing. *PNAS*, 105(49):19270–19275, 2008.

[17] Pablo A. Iglesias and Peter N. Devreotes. Navigating through models of chemotaxis. *Curr Opin Cell Biol*, 20(1):35–40, 2008.

[18] Wouter-Jan Rappel and Herbert Levine. Receptor noise and directional sensing in eukaryotic chemotaxis. *Physical review letters*, 100(22):228101, 2008.

[19] Jose Negrete Jr, Alain Pumir, Hsin-Fang Hsu, Christian Westendorf, Marco Tarantola, Carsten Beta, and Eberhard Bodenschatz. Noisy oscillations in the actin cytoskeleton of chemotactic amoeba. *Physical review letters*, 117(14):148102, 2016.

[20] Hsin-Fang Hsu, Eberhard Bodenschatz, Christian Westendorf, Azam Gholami, Alain Pumir, Marco Tarantola, and Carsten Beta. Variability and order in cytoskeletal dynamics of motile amoeboid cells. *Physical review letters*, 119(14):148101, 2017.

[21] Raymond E Goldstein. Traveling-wave chemotaxis. *Physical review letters*, 77(4):775, 1996.

[22] Akihiko Nakajima, Shuji Ishihara, Daisuke Imoto, and Satoshi Sawai. Rectified directional sensing in long-range cell migration. *Nature communications*, 5, 2014.

[23] Monica Skoge, Haicen Yue, Michael Erickstad, Albert Bae, Herbert Levine, Alex Groisman, William F Loomis, and Wouter-Jan Rappel. Cellular memory in eukaryotic chemotaxis. *Proc Natl Acad Sci U S A*, 111(40):14448–53, Oct 2014.

[24] Tim Lämmermann, Philippe V Afonso, Bastian R Angermann, Ji Ming Wang, Wolfgang Kastenmüller, Carole A Parent, and Ronald N Germain. Neutrophil swarms require LTB4 and integrins at sites of cell death in vivo. *Nature*, 498(7454): 371–375, 2013.

[25] Bashar Hamza, Elisabeth Wong, Sachin Patel, Hansang Cho, Joseph Martel, and Daniel Irimia. Retrotaxis of human neutrophils during mechanical confinement inside microfluidic channels. *Integrative Biology*, 6(2):175–183, 2014.

[26] KJ Tomchik and Peter N Devreotes. Adenosine 3', 5'-monophosphate waves in Dictyostelium discoideum: a demonstration by isotope dilution–fluorography. *Science*, 212(4493):443–446, 1981.

[27] Sonya Bader, Arjan Kortholt, and Peter JM Van Haastert. Seven Dictyostelium discoideum phosphodiesterases degrade three pools of cAMP and cGMP. *Biochemical Journal*, 402(1):153–161, 2007.

[28] P. Herzmark, K. Campbell, F. Wang, K. Wong, H. El-Samad, A. Groisman, and H. R. Bourne. Bound attractant at the leading vs. the trailing edge determines chemotactic prowess. *PNAS*, 104(33):13349–13354, 2007.

[29] Yuhai Tu and Wouter-Jan Rappel. Adaptation in living systems. *Annual review of condensed matter physics*, 9:183–205, 2018.

[30] Peter N Devreotes, Michael J Potel, and Stephen A MacKay. Quantitative analysis of cyclic AMP waves mediating aggregation in dictyostelium discoideum. *Developmental biology*, 96(2):405–415, 1983.

[31] Marten Postma and Peter JM van Haastert. Mathematics of experimentally generated chemoattractant gradients. In *Chemotaxis*, pages 473–488. Springer, 2009.

[32] Richa Karmakar, Christoph Schich, Nadine Kamprad, Vanessa Scheller, Edgar Gutierrez, Alex Groisman, Wouter-Jan Rappel, and Marco Tarantola. Novel micropatterning technique reveals dependence of cell-substrate adhesion and migration of social amoebas on parental strain, development, and fluorescent markers. *PloS one*, 15(7):e0236171, 2020.

[33] Danny Fuller, Wen Chen, Micha Adler, Alex Groisman, Herbert Levine, Wouter-Jan Rappel, and William F Loomis. External and internal constraints on eukaryotic chemotaxis. *Proc Natl Acad Sci U S A*, 107(21):9656–9659, 2010.

[34] Maurice Sussman. Cultivation and synchronous morphogenesis of Dictyostelium under controlled experimental conditions. In *Methods in cell biology*, volume 28, pages 9–29. Elsevier, 1987.

[35] Kosuke Takeda, Danying Shao, Micha Adler, Pascale G Charest, William F Loomis, Herbert Levine, Alex Groisman, Wouter-Jan Rappel, and Richard A Firtel. Incoherent feedforward control governs adaptation of activated ras in a eukaryotic chemotaxis pathway. *Sci. Signal.*, 5(205):ra2, 2012.

[36] L. Bosgraaf and P. J. Van Haastert. Navigation of chemotactic cells by parallel signaling to pseudopod persistence and orientation. *PLoS ONE*, 4(8):e6842, 2009.

[37] Monica Skoge, Micha Adler, Alex Groisman, Herbert Levine, William F Loomis, and Wouter-Jan Rappel. Gradient sensing in defined chemotactic fields. *Integrative Biology*, 2(11-12):659–668, 2010.

[38] Arpan Bhowmik, Wouter-Jan Rappel, and Herbert Levine. Excitable waves and direction-sensing in Dictyostelium discoideum: steps towards a chemotaxis model. *Physical biology*, 13(1):016002, 2016.

[39] Olaf Ronneberger, Philipp Fischer, and Thomas Brox. U-net: Convolutional networks for biomedical image segmentation. In *International Conference on Medical image computing and computer-assisted intervention*, pages 234–241. Springer, 2015.